Endogenous *N*-acyl taurines regulate skin wound healing

Oscar Sasso[a,1], Silvia Pontis[a,1], Andrea Armirotti[a,2], Giorgia Cardinali[b,2], Daniela Kovacs[b,2], Marco Migliore[a], Maria Summa[a], Guillermo Moreno-Sanz[c], Mauro Picardo[b], and Daniele Piomelli[a,c,d,e,3]

[a]Drug Discovery and Development, Istituto Italiano di Tecnologia, 16163 Genoa, Italy; [b]Cutaneous Physiopathology, San Gallicano Dermatological Institute, Istituto di Ricovero e Cura a Carattere Scientifico, 00163 Rome, Italy; [c]Department of Anatomy and Neurobiology, University of California, Irvine, CA 92697; [d]Department of Pharmacology, University of California, Irvine, CA 92697; and [e]Department of Biological Chemistry, University of California, Irvine, CA 92697

The intracellular serine amidase, fatty acid amide hydrolase (FAAH), degrades a heterogeneous family of lipid-derived bioactive molecules that include amides of long-chain fatty acids with taurine [*N*-acyl-taurines (NATs)]. The physiological functions of the NATs are unknown. Here we show that genetic or pharmacological disruption of FAAH activity accelerates skin wound healing in mice and stimulates motogenesis of human keratinocytes and differentiation of human fibroblasts in primary cultures. Using untargeted and targeted lipidomics strategies, we identify two long-chain saturated NATs—*N*-tetracosanoyl-taurine [NAT(24:0)] and *N*-eicosanoyl-taurine [NAT(20:0)]—as primary substrates for FAAH in mouse skin, and show that the levels of these substances sharply decrease at the margins of a freshly inflicted wound to increase again as healing begins. Additionally, we demonstrate that local administration of synthetic NATs accelerates wound closure in mice and stimulates repair-associated responses in primary cultures of human keratinocytes and fibroblasts, through a mechanism that involves tyrosine phosphorylation of the epidermal growth factor receptor and an increase in intracellular calcium levels, under the permissive control of transient receptor potential vanilloid-1 receptors. The results point to FAAH-regulated NAT signaling as an unprecedented lipid-based mechanism of wound-healing control in mammalian skin, which might be targeted for chronic wound therapy.

FAAH | *N*-acyl taurines | FAEs | fibroblasts | keratinocytes

The skin produces a variety of bioactive lipids that contribute in important ways to cutaneous homeostasis (1, 2). These substances include a family of fatty acyl amides that are structurally and functionally heterogeneous, but share the intracellular serine amidase fatty acid amide hydrolase (FAAH) as a common deactivating enzyme (3). The amides of polyunsaturated fatty acids with ethanolamine, such as anandamide (arachidonoylethanolamide), are endogenous agonists of G protein-coupled cannabinoid receptors (4). In the skin, these lipid amides may act as local modulators of the homeostatic response to injury by regulating the activity of nociceptive terminals and resident immune cells (5–7). Partially overlapping functions may be served by the ethanolamides of saturated and monounsaturated fatty acids, such as palmitoylethanolamide (PEA) and oleoylethanolamide (OEA), which also attenuate nociception and inflammation, but do so by binding to the ligand-operated transcription factor, peroxisome proliferator-activated receptor type-α (PPAR-α) (8). A third group of FAAH substrates, the amides of long-chain fatty acids with taurine [*N*-acyl-taurines (NATs)], has been identified in liver and other rodent tissues (9, 10). The NATs may be produced through enzyme-dependent conjugation of fatty acyl-CoA with taurine—catalyzed by the peroxisomal acyltransferase, acyl-CoA amino acid *N*-acyltransferase-1 (11, 12)—and have demonstrated biological activity in several cellular systems (13, 14). Their roles in physiology remain unknown, however.

In the present study, we report that genetic deletion or pharmacological blockade of FAAH activity causes a profound acceleration of wound healing in mouse skin and stimulates motogenesis of human keratinocytes and differentiation of human fibroblasts in primary cultures. Using a combination of untargeted and targeted lipidomics approaches, we further show that long-chain saturated NATs are primary substrates for FAAH in skin and that the levels of these substances change at the edges of a skin wound as the wound heals, sharply decreasing immediately after the injury to resume as formation of a new epithelial layer begins. Finally, we demonstrate that local administration of synthetic NATs accelerates skin repair in mice and enhances healing-associated responses in human keratinocytes and fibroblasts, through a molecular mechanism that involves phosphorylation of the epidermal growth factor receptor (EGFR), elevation of intracellular calcium, and activation of transient receptor potential vanilloid receptor-1 (TRPV-1).

Results

Immunofluorescence images of intact mouse skin show that FAAH colocalizes with cytokeratin 10 and filaggrin, two proteins that are expressed by epidermal suprabasal keratinocytes (Fig. 1 *A* and *B*), as well as with vimentin, which is produced by dermal fibroblasts (Fig. 1*C*; *SI Appendix*, Fig. S1 demonstrates selectivity of the FAAH antibody). By contrast, no detectable FAAH staining was observed in cells that contain the adipocyte marker, fatty acid-binding protein-4

Significance

Healthy human skin quickly repairs itself when wounded. Skin healing is essential for survival, and it depends on a well-ordered sequence of molecular and cellular events that require the cooperation of several growth-promoting proteins released by skin cells or produced in the extracellular matrix. In the present study, we identify a family of lipid-derived molecules that accelerate the closure of self-repairing skin wounds. These endogenous substances promote migration of epidermal keratinocytes and differentiation of dermal fibroblasts by recruiting intracellular signals similar to those engaged by protein growth factors. Understanding this unprecedented mechanism of wound-healing control may guide new therapeutic approaches to the management of chronic wounds in patients with diabetes, bed-ridden elderly people with pressure ulcers, and immunosuppressed recipients of organ transplants.
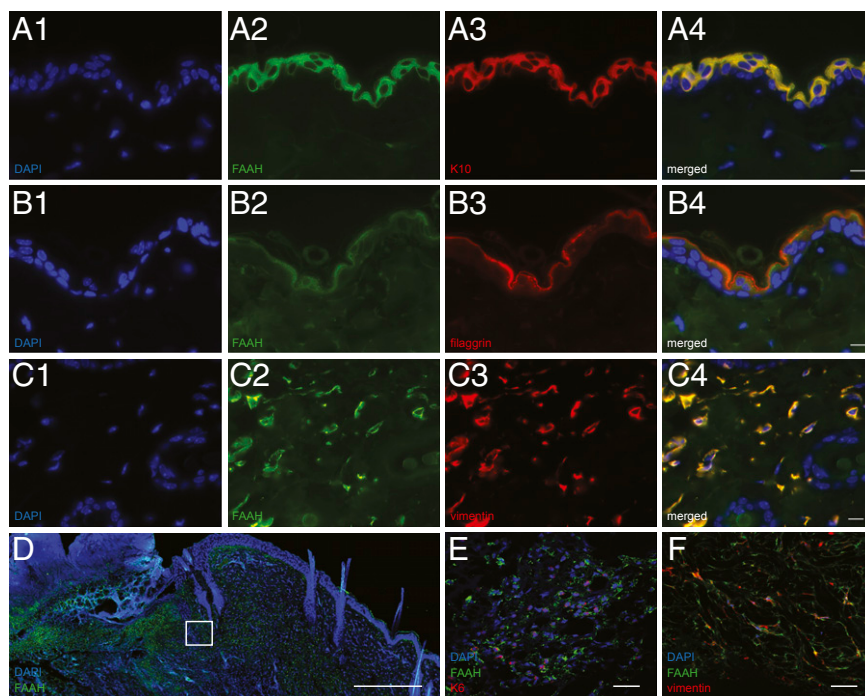
Fig. 1. Localization of FAAH in adult mouse skin. (*A–C*) Representative double immunofluorescence images for FAAH, the keratinocyte markers cytokeratin-10 (K10) (*A1–A4*) and filaggrin (*B1–B4*), and the fibroblast marker vimentin (*C1–C4*) in intact skin. (Scale bars, 10 μm.) (*D*) Immunofluorescence localization of FAAH in wounded skin. The highlighted square is magnified in *E* and *F*, to show the presence of immunoreactive FAAH in keratinocytes (cytokeratin-5; *E*) and fibroblasts (vimentin; *F*). [Scale bars, 500 μm (*D*) and 20 μm (*E* and *F*)]. FAAH is shown in green, and all other markers in red; colocalization (*A4*, *B4*, and *C4*) is shown in yellow; nuclei are stained with DAPI (blue). An antibody selective for FAAH-1, the only FAAH isoform present in rodent tissues, was used in these experiments.

(*SI Appendix*, Fig. S2). Western blot analyses of epidermis and dermis, separated mechanically after dispase digestion, confirmed that both tissue layers contained FAAH (*SI Appendix*, Fig. S3). To test whether the distribution pattern of the enzyme is altered after tissue damage, we inflicted full-thickness excision wounds on the dorsal skin of mice and, 7 d later, localized FAAH by immunofluorescence (Fig. 1*D*). In addition to keratinocytes (Fig. 1*E*), spindle-shaped cells expressing both FAAH and vimentin, most likely fibroblasts, were visible throughout the granulation tissue and dermal layer surrounding the wound (Fig. 1*F*). These results confirm previous data documenting the presence of FAAH in cellular components of cutaneous tissue (1, 15) and point to the possibility that this enzyme might participate in skin repair.

In support of that idea, we found that excision wounds healed more rapidly in mice lacking the Faah gene than they did in wild-type control animals (Fig. 2 *A*, *F*, and *G*). This trait was not attributable to developmental compensation, because it was phenocopied by daily topical administration of the compound URB597 [0.03–3% (wt/vol)], a potent FAAH inhibitor (16), which accelerated wound closure in a dose-dependent manner (Fig. 2 *B*, *H*, and *I*). Histological and morphometric analyses of skin sections prepared 7 d after wounding confirmed the macroscopic findings: Hematoxylin/eosin staining showed that wound depth area (Fig. 2*C*) and distance between migration tongues (Fig. 2*D*) were reduced in mice treated with URB597 [3% (wt/vol)] relative to vehicle-treated controls. These effects were associated with higher cell density in the dermis (Fig. 2*E*) and greater recovery of normal skin structure (Fig. 2 *J* and *K*). Similar results were obtained in Faah$^{-/-}$ mice (Fig. 2*L* and *SI Appendix*, Fig. S4). Epithelialization in the absence of FAAH was cytologically normal, as shown by immunostaining for three distinct epidermal differentiation markers: cytokeratin 5, cytokeratin 10, and filaggrin (*SI Appendix*, Fig. S5).

Next, we examined whether pharmacological or genetic removal of FAAH activity influences recovery of skin tissue structure and function after a surgical intervention. Incisions were made through skin, fascia, and muscle of the plantar aspect of a mouse paw and were apposed with a suture (17). Recovery was assessed by using a scale that evaluated, under blinded conditions, the following features: wound closure and scar formation (markers of skin healing); erythema, edema, and presence of pus (markers of local inflammation); and nocifensive responding to heat or light touch (markers of pain). As expected from previous work (18), oral administration of URB597 (1, 3, or 10 mg/kg, once daily) caused dose-dependent anti-inflammatory and antinociceptive effects, which were accompanied by a dramatic enhancement of wound closure (Fig. 3*A*). At the highest dose of URB597 (10 mg/kg), ostensibly complete closure occurred within 24 h of surgery (Fig. 3*A*). Genetic FAAH deletion exerted similar effects (Fig. 3*B*). The finding that interruption of FAAH activity promotes the closure of excisional wounds and speeds up organ recovery after surgery points to the possibility that endogenous FAAH substrates might be implicated in skin healing.

The skin contains a complex array of lipid constituents (19), including various bioactive fatty acid amides that may be hydrolyzed by FAAH (3). To identify a preferred substrate for this enzyme in skin, which might participate in the healing response, we first conducted an untargeted lipidomics survey of cutaneous tissue samples obtained from Faah$^{-/-}$ and wild-type mice. Lipid extracts were analyzed by high-resolution liquid chromatography mass spectrometry (LC-MS) in the negative- and positive-ion modes. Comparisons carried out by principal component analysis (PCA) revealed clear differences in skin lipid composition between the two strains (negative-ion mode, Fig. 4*A*; positive-ion mode, *SI Appendix*, Fig. S6). To search for individual molecules that contribute to such differences, we reexamined the LC-MS data using an orthogonal projection to a latent structure-discriminant analysis (OPLS-DA) model (20, 21). The analysis pointed to several lipid species that distinguished the skin of Faah$^{-/-}$ mutants from that of wild-type controls (Fig. 4*B*).
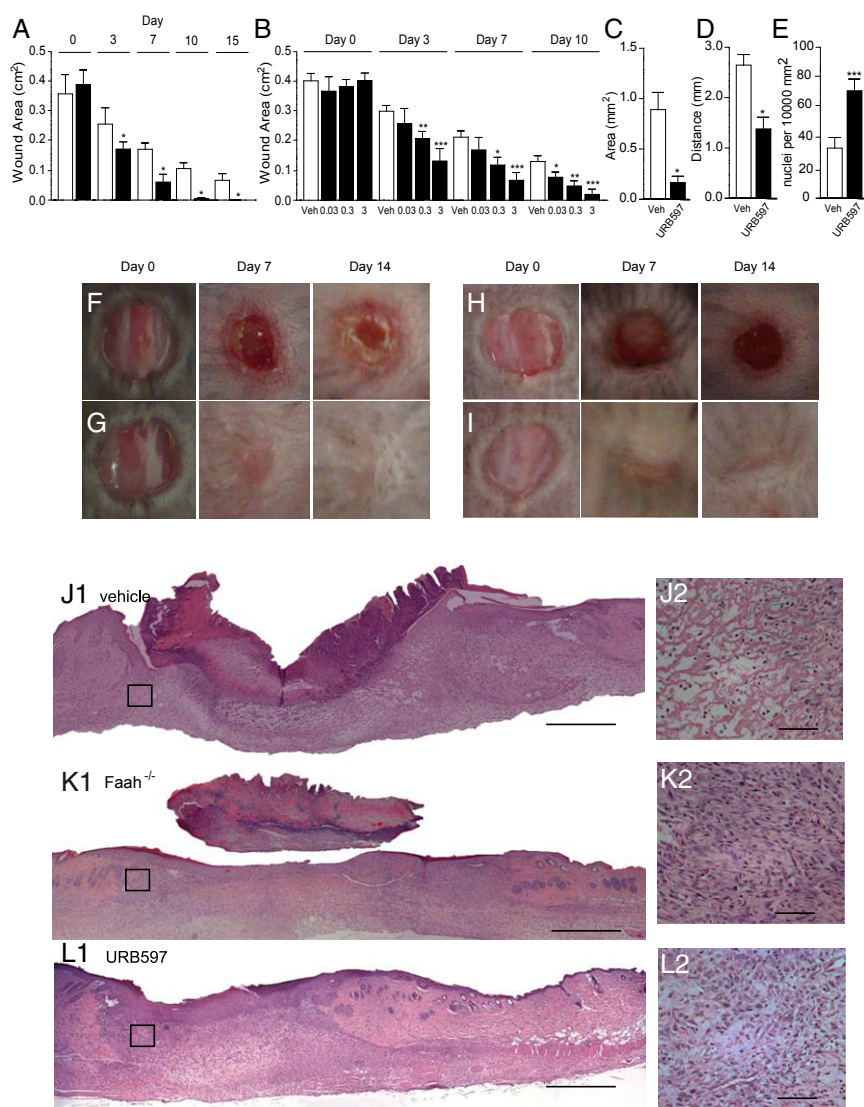
Fig. 2. FAAH regulates healing of excisional skin wounds in mice. (*A*) Time course (days) of wound healing in wild-type mice (open bars) and Faah⁻/⁻ mice (filled bars). (*B*) Time course of wound healing in wild-type mice treated with vehicle (open bars) or with various topical doses (%; wt/vol) of the FAAH inhibitor URB597 (filled bars). (*C–E*) Morphometric analyses showing the effects of vehicle (open bars) or URB597 (3%, wt/vol) (filled bars) on wound area (*C*), distance between migration tongues (*D*), and cell density in the dermis (*E*). (*F–I*) Representative images illustrating skin wound healing in drug-naïve wild-type mice (*F*), drug-naïve Faah⁻/⁻ mice (*G*), and wild-type mice treated either with vehicle (*H*) or URB597 (3%, wt/vol; *I*). (*J–L*) Hematoxylin/eosin staining of skin sections from drug-naïve wild-type mice (*J1*), drug-naïve Faah⁻/⁻ mice (*K1*), and wild-type mice treated with URB597 (3%, wt/vol; *L1*). The highlighted squares are magnified in *J2*, *K2*, and *L2*. [Scale bars, 500 μm (*J1*, *K1*, and *L1*) and 50 μm (*J2*, *K2*, and *L2*).] Skin sections were prepared 7 d after wounding. Data are expressed as mean ± SEM (*n* = 9). *P < 0.05; **P < 0.01; ***P < 0.001 (compared with vehicle or wild-type mice, two-tailed Student's *t* test).

Among the analytes that were most significantly overrepresented in Faah⁻/⁻ animals (black dots at the lower left of the sigmoidal plot), two NAT species were tentatively identified from their accurate mass-to-charge ratio (*m/z*): *N*-tetracosanoyl-taurine [NAT (24:0)] and *N*-eicosanoyl-taurine [NAT(20:0)]. In a subsequent experiment, the structural identities of these compounds were unambiguously confirmed by comparing their LC-MS properties with those of authentic standards synthesized in the laboratory (Fig. 4 *C–F*; tandem mass spectra of tissue-derived and synthetic NATs are shown in *SI Appendix,* Fig. S7). To obtain a more accurate quantification of NAT species in the skin, and improve the sensitivity of our assay, in another experiment we focused our MS analyses on a mass range (*m/z* = 50–600) that encompassed all known FAAH substrates. The results confirmed that FAAH deletion is accompanied by a striking increase in skin levels of NAT(24:0) and NAT(20:0) [quantified by using NAT(17:0) as

internal standard] (Fig. 4 *G* and *H*). In addition, these more focused analyses revealed substantial elevations in other NATs with saturated carbon chains composed of 20–26 units (negative-ion mode, *SI Appendix,* Table S1; positive-ion mode, *SI Appendix,* Table S2). Monounsaturated and polyunsaturated NAT species were relatively rare, but could also be detected [e.g., NAT(24:1)]. As expected, significant differences between wild-type and Faah⁻/⁻ mice were also observed in the levels of anandamide, PEA and OEA (quantified using a standard curve and deuterated internal standards) (Fig. 4 *I–K*). The analyses outlined above identify long-chain saturated NATs as primary substrates for FAAH in mouse skin.

Since their discovery in 2005 (22), NATs have attracted only limited research interest, and their biological functions remain unknown. Because these lipid amides are uniquely overrepresented in the skin of Faah⁻/⁻ mice, we hypothesized that they might be implicated in the enhanced healing response associated
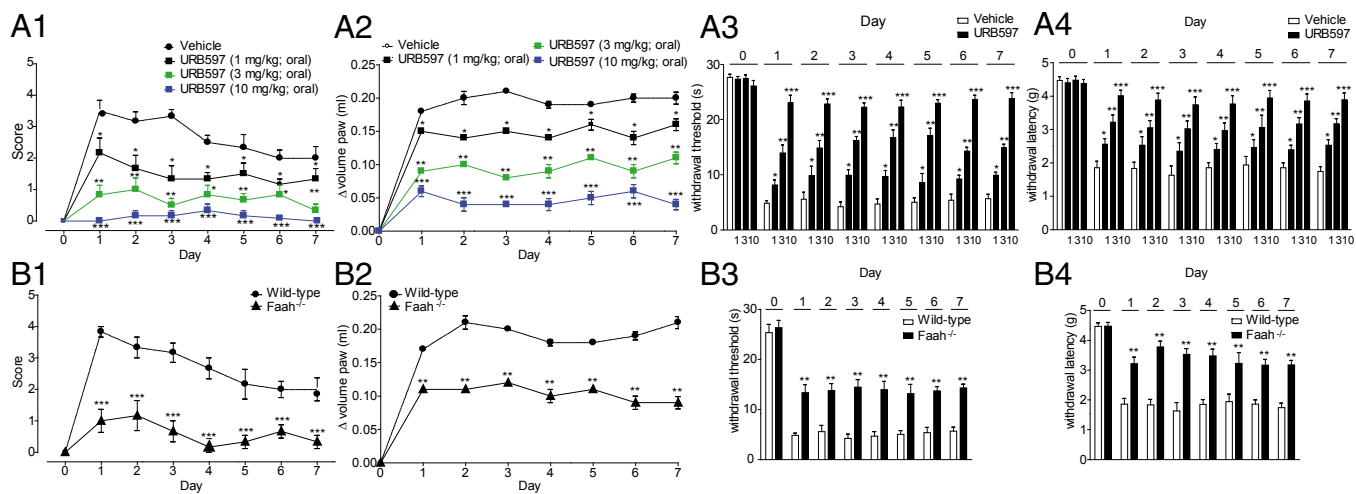
Fig. 3. FAAH regulates recovery of paw tissue structure and function after a surgical incision. (*A*) Time course (days) of recovery in mice treated with the FAAH inhibitor URB597 (1, 3, and 10 mg/kg, oral). The following parameters were evaluated: wound closure and scar formation (*A1*), paw edema (*A2*), heat hyperalgesia (*A3*), and mechanical allodynia (*A4*). (*B*) Time course of recovery in wild-type and Faah$^{-/-}$ mice: wound closure (*B1*), edema (*B2*), hyperalgesia (*B3*), and allodynia (*B4*). Data are expressed as mean ± SEM (n = 9). *$P < 0.05$; **$P < 0.01$; ***$P < 0.001$ (compared with vehicle or wild-type mice, two-way ANOVA).

with removal of FAAH regulation. As a first test of this idea, we asked whether injury alters NAT levels in skin, as seen with protein growth factors that stimulate skin repair (23). We removed the edges of full-thickness excision wounds, or equivalent samples from intact skin, and measured NAT levels in lipid extracts by targeted LC-MS analyses. We found that NAT(24:0) and NAT(20:0) content was substantially lower at the margins of a freshly inflicted wound, relative to nonwounded skin (Fig. 4 *L* and *M*). NAT levels returned to baseline 3 d later (Fig. 4 *L* and *M*); that is, at a time when local inflammation subsides and wound epithelialization begins (24). No such changes were observed with two other NAT species: *N*-stearoyl-taurine [NAT(18:0)], which only showed a transient decrease 6 h after wounding (Fig. 4*N*), and *N*-oleoyl-taurine [NAT(18:1)], the levels of which remained unaltered (Fig. 4*O*).

If endogenous NATs contribute to skin repair, as the time-course of their mobilization at wound sites suggests, then topical administration of these compounds should speed up healing. Consistent with this prediction, macroscopic and histological measurements showed that application of low doses of synthetic NAT(24:0) or NAT(20:0) [0.001–0.1% (wt/vol)] caused a steep acceleration of the healing response, compared with vehicle alone (Fig. 5 *A* and *B*; histological analyses are shown in *SI Appendix*, Fig. S8). In addition to these two NAT species, we examined the effects of three other FAAH substrates present in skin: the endogenous PPAR-α agonists, PEA and OEA, and the endocannabinoid anandamide. PEA and OEA stimulated wound closure, but at dosages that were ~300 times higher than equally effective doses of NAT(24:0) or NAT(20:0) (the effects of PEA are shown in Fig. 5*C*; those of OEA are in *SI Appendix*, Fig. S9). By contrast, anandamide [1% or 3% (wt/vol)] had no measurable impact on healing speed (Fig. 5*D*). Collectively, the results outlined above suggest that endogenous NAT(24:0) and NAT(20:0) promote skin repair in mice in a potent and selective manner.

Cutaneous healing differs between rodents and humans (25). To begin to explore the roles of FAAH-regulated NAT mobilization in human skin, we examined the consequences of pharmacological FAAH blockade on the motogenic response of human keratinocytes. Confluent monolayers of foreskin keratinocytes in primary cultures were scraped to create a cell-free space, and cell migration through the space was evaluated 18 h later (26). Inclusion of the FAAH inhibitor URB597 (0.5 or 1 μM) in the incubation medium produced a marked increase in keratinocyte migration (Fig. 6*A*). Quantitative measures showed that the surface area covered by the

cells was greater in cultures treated with URB597 than in those that had only received vehicle (percentage of edge distance reduction: URB597, 63.1 ± 11.5%; vehicle, 19.3 ± 3.9%; mean ± SD) (Fig. 6*B*). By contrast, URB597 had no detectable effect on keratinocyte proliferation: The percentage of keratinocytes expressing the Ki67 protein, a marker of cell proliferation, was not changed by addition of the drug (Fig. 6*C*). Similar to URB597, application of exogenous NAT(20:0) (0.1 or 1 μM) strongly stimulated keratinocyte migration (Fig. 6 *D* and *E*) without influencing proliferation (Fig. 6*F*). Next, we asked whether FAAH inhibition might promote the differentiation of fibroblasts into myofibroblasts, a transition that is essential for wound contraction and synthesis/remodeling of the extracellular matrix (23, 27). Immunofluorescence studies in primary cultures of human fibroblasts showed that URB597 (0.5 or 1 μM, 48 h) increased the expression of α-smooth muscle actin, a myofibroblast marker (28) (Fig. 6 *G* and *H*). The FAAH inhibitor also enhanced expression of procollagen type I, an important component of the extracellular matrix (Fig. 6 *I* and *J*). The results suggest that FAAH-regulated NAT signaling contributes to the control of repair-associated responses in human keratinocytes and fibroblasts.

Lastly, we probed the molecular mechanism through which long-chain saturated NATs stimulate wound healing. Prior studies have shown that polyunsaturated NATs, such as *N*-arachidonoyl-taurine [NAT(20:4)], activate TRPV-1 and other members of the TRP family of cation channels (10). These effects were reported to occur, however, at concentrations (EC$_{50}$ ~ 20 μM) that are unlikely to be physiologically relevant in the skin, where even the most abundant NAT species, NAT(24:0) and NAT(20:0), do not exceed single-digit micromolar levels (Fig. 4 *L* and *M*). When added to the culture medium at realistic concentrations (0.01–3 μM), NAT(24:0) and NAT(20:0) failed to elevate calcium levels in Chinese hamster ovary (CHO) cells engineered to express human TRPV-1 (*SI Appendix*, Fig. S10). By contrast, the vanilloid agonist capsaicin elicited, in the same cells, robust calcium transients with an EC$_{50}$ of 3.1 nM. Furthermore, a screening campaign revealed no significant effect of NAT(20:0) (10 μM) on a panel of 105 functionally important proteins, including enzymes involved in lipid metabolism and inflammation, neurotransmitter and hormone receptors, transporters, and ion channels (*SI Appendix*, Table S3). These negative results prompted us to turn our attention to two cellular signals—phosphorylation of the EGFR and mobilization of intracellular calcium—which are known to be associated with skin healing (29, 30). The addition of URB597 (1 μM) to the medium of primary cultures
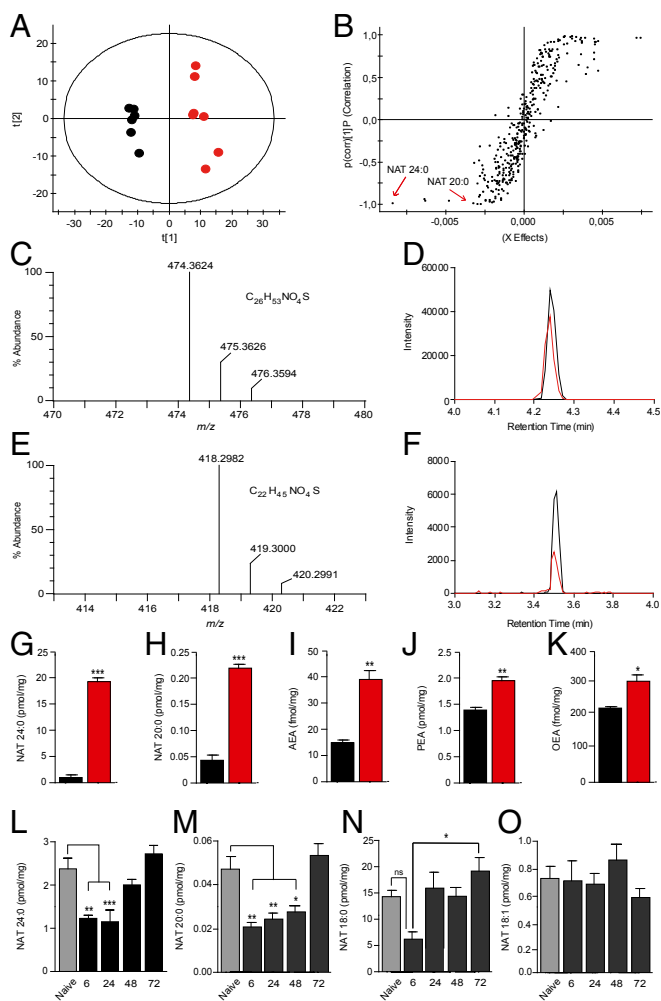
Fig. 4. Identification of preferred FAAH substrates in mouse skin. (A) Score plot from PCA of skin lipidomics profiles of wild-type mice (black circles) and Faah⁻/⁻ mice (red circles) acquired in negative-ion mode; t[1] and t[2], principal component 1 and 2, respectively. (B) Sigmoidal plot of OPLS-DA analysis of the negative-ion dataset. Signals strongly contributing to class separation are those found at the bottom left (Faah⁻/⁻ mice) or top right (wild-type mice) of the plot. Details for each signal are reported in SI Appendix, Table S1. (C–F) High-resolution mass spectra, calculated molecular formulae, and LC/MS tracings for native and synthetic NAT(24:0) (C and D) and NAT(20:0) (E and F). Native compounds are shown in red, authentic standards are shown in black. (G–K) Quantification of NAT(24:0) (G), NAT(20:0) (H), anandamide (AEA) (I), PEA (J), and OEA (K) in skin of wild-type (black bars) and Faah⁻/⁻ (red bars) mice. (L–O) Time course of changes in the levels of NAT(24:0) (L), NAT(20:0) (M), NAT(18:0) (N), and NAT(18:1) (O) in skin tissue surrounding excision wounds (solid bars) or from unwounded mice (shaded bars). Data are expressed as mean ± SEM ($n = 3$). *$P < 0.05$; **$P < 0.01$; ***$P < 0.001$ (compared with wild-type mice, two-tailed Student's t test; $n = 5$); #$P < 0.05$ (one-way ANOVA); ns, not significant.

of human keratinocytes caused a rapid induction of EGFR phosphorylation on tyrosine 1,068 (Fig. 7 A and B), which is essential for downstream signaling at this receptor (31). Similar results were obtained with NAT(20:0) (1 μM) (Fig. 7 A and B). Increased EGFR phosphorylation was accompanied by a slowly developing rise in intracellular calcium levels (Fig. 7C). Interestingly, the effects of URB597 on EGFR phosphorylation and calcium activity were abrogated in the presence of the selective TRPV-1 antagonist AMG9810 (5 μM) (Fig. 7 A–C), which is suggestive of an obligatory role for TRPV-1 in NAT-dependent signaling. Consistent with this idea, we found that (i) mice lacking the *Trpv1* gene were completely insensitive to the application of URB597 [3% (wt/vol), once daily]

(Fig. 7D) or NAT(20:0) [0.01% (wt/vol), once daily] (Fig. 7E); and (ii) topical treatment with AMG9810 [0.3% or 1% (wt/vol), once daily] prevented the wound healing acceleration observed in Faah⁻/⁻ mice (Fig. 7F). We interpret these results as indicating that long-chain saturated NATs stimulate wound closure in mouse and human skin by stimulating EGFR phosphorylation and calcium mobilization, under the permissive control of TRPV-1.

Discussion

The repair of skin wounds in mammals requires the participation of multiple cell lineages, which are sequentially recruited during the successive phases of blood clotting, inflammation, proliferation, and remodeling (32). Secreted proteins such as EGF, transforming growth factor-α and -β, and keratinocyte growth factor are important players in this well-ordered series of events (32). In the present study, we identify FAAH-regulated long-chain saturated NATs as an unprecedented lipid-derived signal that may act in cooperation with protein growth factors to promote normal skin healing. The results show that FAAH—an intracellular membrane-bound serine hydrolase that degrades bioactive lipid amides such as anandamide, PEA, and OEA (5)—is expressed by keratinocytes and resident fibroblasts in cutaneous tissue of healthy adult mice. Our findings further indicate that genetic or pharmacological interventions that disable FAAH cause a profound acceleration in the repair of skin wounds. This result, unexpected from the known biology of FAAH, suggests that an important role of this enzyme in skin may be to deactivate an endogenous lipid substrate, or substrates, that stimulates wound closure. In an effort to identify such substrate(s), we compared the skin lipidome of wild-type and Faah⁻/⁻ mice using a combination of untargeted and targeted analytical strategies. The results of these experiments demonstrate that long-chain saturated NATs, such as NAT(24:0) and NAT(20:0), are major substrates for FAAH in mouse skin and that formation of these compounds in tissue surrounding a wound is turned off after damage to be reinstated at the onset of the proliferation phase of healing (24). The possibility, suggested by these results, that FAAH-regulated NAT signaling might be involved in skin repair was confirmed by showing that application of synthetic NAT(24:0) or NAT(20:0) accelerates wound closure. Finally, supporting the translational relevance of our results, we found that FAAH inhibition or application of exogenous NATs stimulates migration of human keratinocytes and differentiation of human fibroblasts into myofibroblasts, two critical steps in skin repair (33, 34).

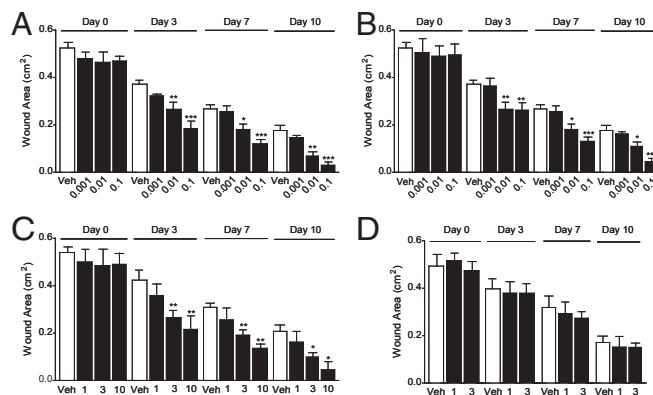**Fig. 5.** Synthetic NATs accelerate skin healing in mice. (A and B) Time course (days) of wound closure in wild-type mice treated daily with topical applications of vehicle (open bars) or synthetic NAT(24:0) (A), NAT(20:0) (B), PEA (C), or anandamide (D) (%; filled bars). Data are expressed as mean ± SEM ($n = 9$). *$P < 0.05$; **$P < 0.01$; ***$P < 0.001$ (compared with vehicle or wild-type mice, two-tailed Student's t test).
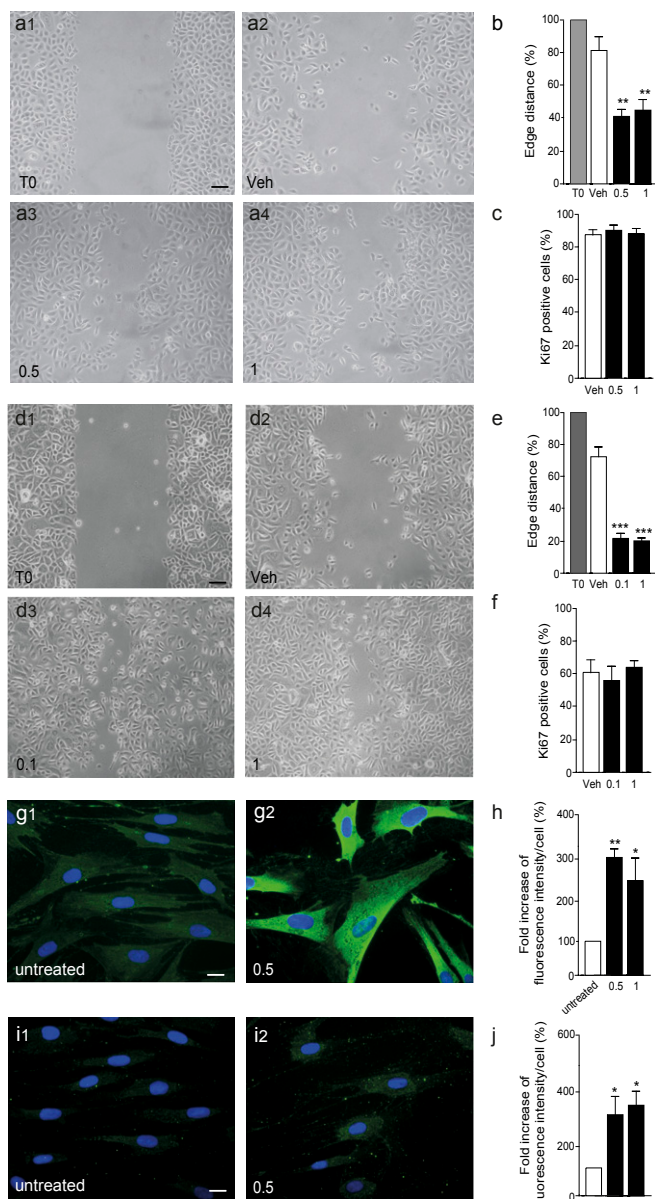
Fig. 6. FAAH controls human keratinocyte migration and human fibroblasts transdifferentiation into myofibroblasts. (*A* and *B*) Representative image illustrating the motogenic effects of the FAAH inhibitor URB597 (0.5 or 1 μM; 18 h) in primary cultures of human keratinocytes (*A*) and quantitative analysis of leading edges distance (*B*). Data are expressed as percent of vehicle-treated control cultures (mean ± SEM). (*C*) Effects of URB597 (48 h) on keratinocyte proliferation. (*D*–*F*) Effects of synthetic NAT(20:0) on keratinocyte migration (18 h) (*D* and *E*) and keratinocyte proliferation (48 h) (*F*). (*G*–*J*) Effects of URB597 (0.5 μM, 48 h) on the expression of α-smooth muscle actin (*G* and *H*) and procollagen type I (*I* and *J*) in human fibroblasts. Data are expressed as mean ± SEM (*n* = 3). (Scale bars, 20 μm.) *$P < 0.05$; **$P < 0.01$; ***$P < 0.001$ (compared with vehicle mice, two-tailed Student's *t* test).

Initial investigations into the signal transduction mechanism underlying the prohealing effects of long-chain saturated NATs revealed the participation of two molecular events—EGFR phosphorylation on tyrosine 1,068 and induction of intracellular calcium transients—which are known to contribute in important ways to epidermal repair (35). Moreover, we observed that EGFR phosphorylation and calcium mobilization depend on the activity of the cation channel, TRPV-1, which has been implicated in the control of directional keratinocyte migration (36). The latter result

is consistent with the ability of the TRPV-1 agonist, capsaicin, to stimulate wound closure (36). Unlike capsaicin, however, long-chain saturated NATs do not directly activate TRPV-1, at least at physiologically relevant concentrations [~2.5 μM for NAT(24:0) and ~0.05 μM for NAT(20:0)], pointing to the existence of an as-yet-unidentified receptor, presumably expressed in keratinocytes and fibroblasts, which mediates the actions of NATs. Identifying this hypothetical receptor is an important objective for future research.

Two additional questions raised by the present study pertain to the signals controlling NAT mobilization after wounding and the interplay between NATs and other bioactive lipid amides that are deactivated by FAAH (5). These questions are likely to be interconnected. Previous studies have shown that two FAAH substrates present in the skin, PEA and OEA, modulate local inflammatory responses by activating the nuclear receptor PPAR-α (8, 37). Like NAT formation after wounding, the production of PEA and OEA is suppressed by proinflammatory stimuli (38–40), suggesting that different classes of lipid amides may regulate distinct phases of the healing response in a coordinated manner. Answering these questions may help uncover possible roles of NAT-mediated signaling in pathological impairments of skin repair, such as those consequent to aging, diabetes, and immunosuppression, and might guide the development of new strategies for the management of chronic nonresolving wounds.

Materials and Methods

Chemicals. AMG9810, anandamide, OEA, and PEA were purchased from Sigma-Aldrich. URB597 (cyclohexylcarbamic acid 3′-carbamoylbiphenyl-3-yl ester) was synthesized and characterized in house as described (41). NATs were prepared as described below.

Synthesis of NATs. Fatty acids (3 mmol; Zentek) were suspended in thionyl chloride (30 mL) and stirred at reflux for 17 h. Excess thionyl chloride was evaporated under reduced pressure, and the liquid obtained was added dropwise to a solution of taurine (1.88 g, 15 mmol) and triethylamine (2.1 mL, 15 mmol) in water (100 mL) at 0 °C. The mixture was stirred for 1 h and then basified with sodium hydroxide. The solid formed was filtered under vacuum, and the residue was recrystallized from methanol/water to obtain the title compound. NMR experiments were run on a Bruker Avance III 400 system (400.13 MHz for ^{1}H and 100.62 MHz for ^{13}C), equipped with a broadband inverse probe and *z*-gradients. Spectra were acquired by using deuterated dimethyl sulfoxide (DMSO-*d6*) as solvent. Chemical shifts for ^{1}H and ^{13}C spectra were recorded in parts per million (ppm) by using the residual nondeuterated solvent as internal standard. Data are reported as follows: chemical shift (ppm), multiplicity (indicated as bs, broad signal; s, singlet; d, doublet; t, triplet; q, quartet; p, quintet; and m, multiplet), coupling constants (*J*) in Hertz, and integrated intensity. Sodium 2-(icosanoylamino)ethanesulfonate: white solid (76%). ^{1}H NMR (400 MHz, DMSO-*d6*, 300 K) δ 7.65 (t, J = 5.3 Hz, 1H), 3.33–3.23 (m, 2H), 2.56–2.45 (m, 2H), 2.01 (t, J = 7.4 Hz, 2H), 1.46 (p, J = 7.5 Hz, 2H), 1.32–1.15 (m, 32H), 0.86 (t, J = 6.7 Hz, 3H). ^{13}C NMR (101 MHz, DMSO-*d6*, 300 K) δ 171.80, 50.61, 35.61, 35.46, 31.29, 29.02 (12xC), 28.80, 28.68, 25.19, 22.09, 13.96. Sodium 2-(tetracosanoylamino)ethanesulfonate: white solid (81%). ^{1}H NMR (400 MHz, DMSO-*d6*, 350 K) δ 7.45 (bs, 1H), 3.32 (q, J = 6.8 Hz, 2H), 2.54 (t, J = 7.0 Hz, 2H), 2.02 (t, J = 7.4 Hz, 2H), 1.59–1.44 (m, 2H), 1.25 (m, 40H), 0.96–0.79 (m, 3H). ^{13}C NMR (101 MHz, DMSO-*d6*, 350 K) δ 171.83, 50.65, 36.23, 35.64, 31.31, 29.03 (16xC), 28.85, 28.72, 25.24, 22.11, 14.74. Sodium 2-(heptadecanoylamino)ethanesulfonate: white solid (88%). ^{1}H NMR (400 MHz, DMSO-*d6*, 300 K) δ 7.67 (bs, 1H), 3.32–3.21 (m, 2H), 2.55–2.48 (m, 2H), 2.00 (t, J = 6.2 Hz, 2H), 1.45 (p, J = 6.7 Hz, 2H), 1.36–0.99 (m, 24H), 0.85 (t, J = 7.0 Hz, 3H). ^{13}C NMR (101 MHz, DMSO-*d6*, 300 K) δ 171.68, 50.65, 35.63, 35.48, 31.35, 29.10 (8xC), 29.01, 28.86, 28.76, 28.72, 25.25, 14.03.

Animals. Experiments were carried out on male adult C57BL6/6J mice (Charles River), Faah$^{-/-}$ mice (University of California, Irvine; bred from founders gifted by B. Cravatt, Departments of Cell Biology and Chemistry, The Skaggs Institute for Chemical Biology, The Scripps Research Institute, La Jolla, CA), and Trpv1$^{-/-}$ mice (Charles River) weighing 25–30 g. Faah$^{-/-}$ and Trpv1$^{-/-}$ mice were back-crossed onto C57BL6/6J background for >10 generations. The animals were housed in groups of five in ventilated cages with free access to food and water. They were maintained under a 12-h light/dark cycle at controlled temperature (21 ± 1 °C) and relative humidity (55 ± 10%). All experiments were performed in accordance with the Ethical Guidelines of the International Association for the Study of Pain
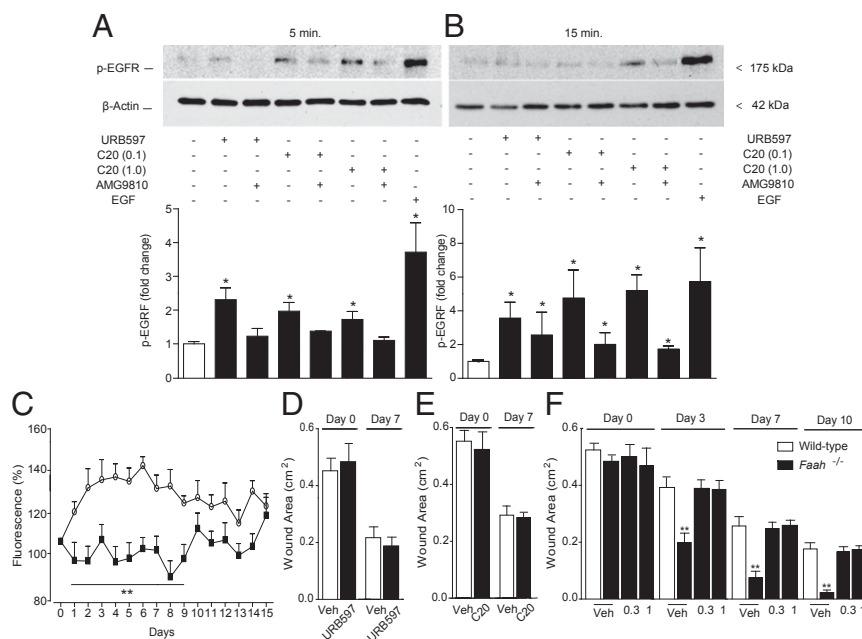
Fig. 7. Signal transduction events initiated by FAAH-regulated NAT signaling in human keratinocytes. (*A* and *B*) Western blot analyses of primary cultures of human keratinocytes 5 min (*A*) and 15 min (*B*) after addition of the FAAH inhibitor URB597 or synthetic NAT(20:0) (C20 0.1 and 1 μM), in the absence or presence of the TRPV-1 antagonist AMG9810 (5 μM). (*A, Upper*, and *B, Upper*) Representative blots. (*A, Lower*, and *B, Lower*) Quantification of data from three independent experiments. EGF was used as positive control and β-actin as loading control. (*C*) Intracellular calcium levels (fluo-3 fluorescence) in human keratinocytes incubated with URB597 (1 μM; open circles) or URB597 plus TRPV-1 antagonist AMG9810 (5 μM; filled squares). Vehicle and AMG9810 had no effect on calcium levels when applied alone. (*D*) Effects of vehicle (open bars) or URB597 [3% (wt/vol); filled bars] on wound healing in *Trpv1*−/− mice. (*E*) Effects of vehicle (open bars) or NAT(20:0) [0.01% (wt/vol); filled bars] on wound healing in *Trpv1*−/− mice. In *D* and *E*, wound areas were measured 0 and 7 d after wounding. (*F*) Time-course of wound healing in wild-type mice treated with vehicle (open bars) and *Faah*−/− mice (filled bars) treated with vehicle or AMG9810 [0.3 or 1% (wt/vol)]. Data are expressed as mean± SEM (*n* = 3 for keratinocyte experiments, and *n* = 9 for in vivo experiments). *$P < 0.05$; **$P < 0.01$; ***$P < 0.001$ (compared with controls).

and were approved by Italian regulations on protection of animals used for experimental and other scientific purposes (D.M. 116192), as well as with European Economic Community regulations (O.J. of E.C. L 358/1 12/18/1986).

Primary Cell Cultures. Primary cultures of keratinocytes and fibroblasts were prepared from human neonatal foreskin, as described (42), and maintained in Medium 154 (Invitrogen) supplemented with human keratinocyte growth supplement (Invitrogen) plus antibiotics and calcium chloride (0.07 mM), and DMEM with 10% FBS and antibiotic, respectively. Three keratinocyte and fibroblast pools, each coming of two donors, were used. The study was approved by the medical ethical committee of the San Gallicano Dermatologic Institute and was conducted according to the principles of the Declaration of Helsinki. Participants' custodians gave their written informed consent. URB597 was dissolved in DMSO, and NAT(20:0) was dissolved in a mixture of PEG:ethanol [55%/45% (vol/vol)]. Keratinocytes were maintained in growth factor-free medium for 24 h and treated with URB597 or NAT(20:0) for the indicated times. Fibroblasts were maintained in DMEM without FBS for 24 h and treated with URB597 for 48 h. Control cells were treated with equal volumes of the respective vehicles.

Separation of Epidermis from Dermis. Fresh mouse skin samples (200–300 mg) were incubated in calcium- and magnesium-free PBS containing dispase II (2.5 units/mL) (Sigma-Aldrich) at 4 °C for 24 h (43). At the end of the incubation, individual layers were separated by using surgical tweezers.

Full-Thickness Excisional Wound Model. The dorsum of mice was wounded by using a 6-mm round biopsy punch. The wound area was sterilized with a povidone/iodine solution and treated topically once a day for 14 d, with vehicle (PEG 400, 20 μL), URB597 [0.03–0.3% (wt/vol)], PEA (1–10%), OEA (1–10%), anandamide (1–3%), or an appropriate NAT (0.001–0.1%). The wounds were photographed with a digital camera, and surface areas were measured by using an image-analysis software package (ImageJ; National Institutes of Health). In some experiments, the mice were killed 7 d after wounding, and the wounds were harvested along with the underlying muscle and 3 mm of adjacent unwounded skin. The tissues were fixed in 4% paraformaldehyde (PFA) and embedded in paraffin; 4-μm serial sections were collected. The section presenting the largest wound diameter was defined as wound center.

Sections were stained with hematoxylin/eosin and visualized with an Olympus BX51 microscope. Morphometric analyses were performed by using the Neurolucida software (MBF Bioscience). Wound depth was evaluated by measuring the area defined by the distance between the tip of the migrating epithelial tongues and the surface not covered by the epithelium (25, 44, 45).

Surgical Incision Model. Paw incisions were made as described (17). Briefly, mice were anesthetized with isoflurane delivered via a nose cone. After sterile preparation of the left hind paw, a 0.5-cm longitudinal incision was made through skin and fascia of the plantar surface of the foot with a number-11 scalpel blade. The incision was started 0.2 cm from the proximal edge of the heel and extended distally. The underlying muscle was elevated with curved forceps, leaving the muscle origin and insertion intact. After hemostasis, the skin was apposed with a 6.0 nylon mattress suture, and the wound was covered with antibiotic ointment. Unwounded mice underwent a sham procedure that consisted of anesthesia, antiseptic preparation, and application of the antibiotic ointment. Macroscopic evaluations were conducted every 24 h for 7 d, assigning a 1-point score to each of the following parameters: heat hyperalgesia, mechanical allodynia, redness, visible edema, presence of pus, wound closure, and scar formation (46).

Lipid Extraction. Skin samples were quickly frozen in liquid N_2, finely ground with a mortar, transferred to glass vials, and subjected to lipid extraction according to Bligh and Dyer (47). The organic phases were collected, dried under N_2, and dissolved in methanol/chloroform [9:1 (vol/vol); 0.1 mL] for LC-MS/MS analyses.

Untargeted LC-MS/MS Analyses. Analyses were carried out on a ultraperformance liquid chromatography (UPLC) Acquity system coupled to a Synapt G2 mass spectrometer (both from Waters). Lipids were separated on a reversed-phase C18 T3 column (2.1 × 100 mm; Waters) kept at 55 °C at a flow rate of 0.4 mL/min. The following gradient conditions were used: Eluent A was 10 mM ammonium formate in 60:40 acetonitrile/water, and eluent B was 10 mM ammonium formate in 90:10 isopropyl alcohol/acetonitrile; after 1 min at 30%, solvent B was brought to 35% in 3 min, then to 50% in 1 min, and then to 100% in 13 min, followed by a 1-min 100% B isocratic step and reconditioning to 30% B. Total run time was

22 min. Injection volume was set at 3 μL. Capillary voltages were set at 3 and 2 kV for ESI$^+$ and ESI$^-$, respectively. Cone voltages were set at 30 V for ESI$^+$ and 35 V for ESI$^-$, respectively. Source temperature was 120 °C. Desolvation gas and cone gas (N$_2$) flow were 800 L/h and 20 L/h, respectively. Desolvation temperature was 400 °C. Data were acquired in MS^e mode with MS/MS fragmentation performed in the trap region. This technique enabled the best LC peak sampling by acquiring alternate low-energy/high-energy scans over the entire selected mass range, with no precursor selection in the quadrupole region (48). Low-energy scans were acquired at fixed 4-eV potential, and high-energy scans were acquired with an energy ramp from 25 to 45 eV. Scan rate was set to 0.3 s per spectrum. Scan range was set from 50 to 600 or 1,200 m/z (see text). Leucine enkephalin (2 ng/mL) was infused as lock mass for spectra recalibration.

Raw data from high-resolution LC-MS/MS runs for either polarity (ESI$^+$ or ESI$^-$) were subjected to Pareto-scaled PCA (16) by using the MarkerLynx software (Waters Inc.). Accurate m/z and retention time (RT) values were included in the multivariate analysis and assigned as X-variables (markers). Only markers observed in at least 90% of the experimental replicates were retained. OPLS-DA (20, 21) was performed for both ESI$^+$ and ESI$^-$, and scatter plots were generated. For both polarities, group separation and goodness of fit (R2) as well as goodness of prediction (Q2) were calculated by the software for all of the principal components of OPLS-DA score plot (Comp1: R2 = 0.98 Q2 = 0.81; Comp2: R2 = 0.98 Q2 = 0.83 for ESI+; and Comp1: R2 = 0.99 Q2 = 0.94, Comp2: R2 = 0.99 Q2 = 0.93 for ESI$^-$). To better evaluate the overrepresentation/underrepresentation of individual analytes, a second identical experiment was carried out, focusing the investigation on the mass range of the known and expected FAAH substrates (50–600 m/z). Exogenous NAT(17:0) (not detected in the first untargeted experiment) was added to the chloroform/methanol extraction solvent to a final 0.5 μM concentration. Calibration curves for authentic NAT(20:0) and NAT(24:0) were prepared as described above. After peak detection and realignment using MarkerLynx, the peak area of each signal was normalized by the peak area of NAT(17:0) for ESI$^-$ and by the peak area of free cholesterol for ESI$^+$ (the absolute peak area of which did not significantly change among samples). The marker list generated by the software, reporting all of the detected data (m/z and RT) pairs, was exported to an Excel datasheet for further calculations, following the protocol recently described by González-Domínguez et al. (49). By using the t test function, a P value was calculated for each marker (two-tailed, unpaired, heteroscedastic t test). Signals were preliminarily filtered by P < 0.05 and up-/down-regulation factor (lower than −30% or higher than +30%) and manually processed to eliminate spurious peaks. The accurate mass list was searched against the METLIN web-based algorithm (50, 51), setting an m/z tolerance of 5 ppm and allowing [M-H]$^-$, [M+FA-H]$^-$, and [M-H$_2$O-H]$^-$ for the negative ion mode and [M+H]$^+$, [M+NH4]$^+$, [M+Na]$^+$, [M+K]$^+$, and [M-H$_2$O+H]$^+$ for the positive ion mode as adducted species. Criteria for matching were as follows: accurate mass matching, class-specific RT and adduct type consistency (52), and, whenever possible, accurate MS/MS data, following the indications on MS/MS fragmentation patterns available in the literature (53–56). The lipid species annotated are reported in *SI Appendix*, Table S1 (positive ion mode) and *SI Appendix*, Table S2 (negative ion mode).

Targeted NAT Analysis. Synthetic NAT(17:0) was added to the extraction solvent to a final 0.5 μM concentration, and tissue samples were extracted as described above. A set of calibrators of increasing concentration of synthetic NAT(20:0) and NAT(24:0) (0.1 nM to 10 μM) was prepared and processed along with the samples. NATs were separated on a reversed-phase C8 bridged ethylene hybrid (BEH) column (2.1 × 100 mm) kept at 50 °C and eluted at a flow rate of 0.4 mL/min. The following gradient conditions were used: eluent A was 10 mM ammonium bicarbonate in water, and eluent B was 10 mM ammonium bicarbonate in methanol; after 1 min at 70%, solvent B was brought to 100% in 4 min, followed by a 1-min 100% B isocratic step and reconditioning to 70% B. Total run time was 7 min. Injection volume was 5 μL. Capillary voltage was 2 kV in the ESI mode. Cone voltage was set at 55 V. Source temperature was 120 °C. Desolvation gas and cone gas (N$_2$) flow were 800 and 20 L/h, respectively. Desolvation temperature was 400 °C. Data were acquired in MS^e mode with MS/MS fragmentation performed in the transfer region. Low-energy scans were acquired at fixed 4-eV potential, and high-energy scans were acquired with an energy ramp from 25 to 55 eV. Scan rate was set to 0.3 s per spectrum. Scan range was set from 50 to 600 m/z. Leucine enkephalin (2 ng/mL) was infused as lock mass for spectra recalibration.

Targeted Analysis of Anandamide, PEA, and OEA. Anandamide, OEA, and PEA were measured by LC/MS as described (57). [^{2}H$_4$]-anandamide, [^{2}H$_4$]-OEA, and [^{2}H$_4$]-PEA (Cayman Chemical) were added to the extraction solvent as internal standards, and tissue samples were extracted as described above. The organic extracts were fractionated by open-bed silica gel column chromatography. Anandamide, OEA, and PEA were eluted with chloroform/methanol [9:1 (vol/vol)]. Organic phases

were evaporated under N$_2$ and reconstituted in methanol (0.1 mL). LC/MS analyses were conducted on a Xevo TQ UPLC-MS/MS system equipped with a reversed-phase BEH C18 column (both from Waters), by using a linear gradient of acetonitrile in water. Quantification was performed by monitoring the following multiple reaction monitoring transitions in positive ion mode (parent m/z→daughter m/z, collision energy eV): anandamide 348→62,20; [^{2}H$_4$]-anandamide 352→66,20; OEA 326→62,20; [^{2}H$_4$]-OEA 330→66,20; PEA 300→62,20; [^{2}H$_4$]-PEA 304→66,20. Analyte peak areas were compared with a standard calibration curve (1 nM to 10 μM).

Western Blot Analyses.
FAAH. Skin and liver samples were homogenized in lysis buffer [150 mM sodium chloride, 50 mM Tris·HCl, pH 8.0, 0.5% sodium deoxycholate, 0.1% SDS, and 1% Triton X-100]. The tissue extract were cleared by centrifugation (10 min at 12,000 × g, 4 °C) and denatured in 8% SDS and 5% β-mercaptoethanol at 99 °C for 5 min. Proteins (30 μg) were separated by SDS/PAGE and transferred to poly(vinylidene fluoride) membranes. The membranes were blocked with 5% nonfat dry milk in Tris-buffered saline (TBS) and incubated overnight with anti–FAAH-1 antibody (1:500; Abcam) and anti-GAPDH antibody (1:2,000; Abcam) in TBS containing 1% nonfat dry milk, followed by incubation with horseradish peroxidase (HRP)-linked anti-mouse IgG antibody (1:5,000; Millipore) in TBS containing 0.1% Tween 20 at room temperature for 1 h. Finally, FAAH was visualized with a chemiluminescence kit (Bio-Rad), and images were obtained by using a LAS-4000 lumino-image analyzer system (Fujifilm).
EGFR. Human keratinocytes were lysed in a buffer containing 10 mM Tris (pH 7.4), 50 mM NaCl, 1 mM EDTA, 10 mM KCl, 1% Nonidet P-40, 0.1% SDS, and 0.05% Tween 20, supplemented with protease inhibitors (1 μg/mL aprotinin, 1 μg/mL leupeptin, and 1 mM phenylmethylsulfonyl fluoride) and phosphatase inhibitors (1 mM sodium orthovanadate, 20 mM sodium pyrophosphate, and 5 mM NaF). Protein concentrations were measured with the Bradford reagent (Bio-Rad). Proteins (40 μg) were separated under reducing conditions by SDS/PAGE and transferred to nitrocellulose membranes (Amersham Biosciences). The membranes were blocked with TBS containing 5% milk and 0.05% Tween 20 for 1 h at room temperature and incubated overnight at 4 °C with anti–phospho-EGF Receptor (Tyr-1068) (D7A5) XP rabbit mAb (1:1,000; Cell Signaling Technology,). For p-EGFR detection, a secondary goat anti-rabbit IgG HRP-linked antibody (1:8,00; Cell Signaling Technology) was used. Membranes were washed, and bands were visualized by using an enhanced chemiluminescence reagent (Amersham). A subsequent hybridization with monoclonal anti–β-actin, clone AC-15 (Sigma-Aldrich) was used as a loading control. Protein levels were quantified by measuring the optical densities of specific bands using a GS-800 calibrated image densitometer (Bio-Rad). Western blots are representative of at least three independent experiments.

Immunohistochemistry. Mice were anesthetized with chloral hydrate (400 mg/kg) and perfused transcardially with saline (20 mL) followed by 4% PFA (60 mL). Serial sections derived from PFA-fixed and -embedded blocks were dewaxed in xylene and rehydrated through graded ethanol concentrations to PBS (pH 7.4). Antigen retrieval was achieved by heating sections in 10 mM citrate buffer (pH 6). Tissue sections were then incubated with the following primary antibodies for 16 h at 4 °C: anti–FAAH-1 mouse monoclonal (1:200; Abcam), anticytokeratin 5 rabbit monoclonal (1:500; Abcam), anticytokeratin 10 rabbit monoclonal (1:500; Abcam), antifilaggrin rabbit polyclonal (1:500; Abcam), antivimentin rabbit monoclonal (1:2,000; Abcam), and anti–FABP-4 (1:200; Abcam). Primary antibodies were visualized using anti-rabbit IgG-Alexa Fluor 555 (1:500; Cell Signaling) and anti-mouse IgG-Alexa Fluor 488 (1:500; Cell Signaling). Nuclei were visualized with DAPI (Sigma-Aldrich). Images of naïve mice and of the area surrounding the wound were taken by using a ×60 1.4-numerical aperture objective lens.

Scratch Wound Assay. Keratinocytes were seeded on 35-mm plates and allowed to grow until confluent. They were serum-starved for 24 h, and the bottom of the dish was scraped with a pipette tip (0.2 mL) to create a standardized cell-free area (58). After thorough rinsing, the cells were incubated in culture medium containing URB597 or NAT(20:0). The cultures were fixed with 4% PFA in PBS (30 min at room temperature) immediately after scratch (T0) and after 18 h of treatment. Images were recorded by using an Axiovert 25 inverted microscope (Carl Zeiss) and a Power Shot G5 digital camera (Canon). Migration was quantitated by measuring the recovered scratch area as reduction of edge distance. Values are expressed as percentage and represent the mean value ± SEM from three independent experiments. Keratinocytes and fibroblasts were fixed in 4% PFA for 30 min at room temperature followed by 0.1% Triton X-100. They were incubated with the following primary antibodies: anti-Ki67 polyclonal antibody (1:300 in PBS; Abcam), anti–α-smooth muscle actin (anti–α-SMA; 1:800; Sigma-Aldrich), and

anti-procollagen type I [2Q576] (1:800; Abcam) for 1 h. Primary antibodies were visualized by using anti-rabbit IgG-Alexa Fluor 555 (1:500 in PBS; Cell Signaling Technology), anti-mouse IgG-Alexa Fluor 488 (1:500 in PBS), and anti-rat IgG-Alexa Fluor 488 (1:500 in PBS; Invitrogen). Cell proliferation was evaluated as percentage of cycling Ki67-positive nuclei with respect to total cells counting at least 200 cells from 10 different microscopic fields. Values are expressed as percentage and represent the mean value ± SEM from three independent experiments. Quantitative analysis of α-SMA and procollagen type I expression was performed by using the AxioVision software (v4.7.1; Carl Zeiss), and values represent the percentage of mean fluorescence intensity per cell ± SEM from three different experiments. Graphs represent the results obtained from one donor. Experiments replicated on a second donor gave comparable results. Nuclei were visualized with DAPI (Sigma-Aldrich). Fluorescence signals were analyzed by recording stained images using a CCD camera (Carl Zeiss).

Calcium Imaging. Human keratinocytes, plated on 24-well plates and cultured overnight, were loaded with the calcium-sensitive dye fluo-3 AM (1.5 μM; Sigma-Aldrich) in loading buffer (135 mM NaCl, 4.5 mM KCl, 1.5 mM CaCl$_2$, 0.5 mM MgCl$_2$, 10 mM Hepes, and 5.6 mM glucose, pH 7.4) for 1 h at 37 °C in the dark. Cells were washed with loading buffer and then treated with NAT

(0.1 μM) alone and in the presence of AMG9810 (5 μM). Immediately after treatments, intracellular calcium was measured with a DTX 880 multimode detector controlled by multimode detector analysis software (v2.0; Beckman Coulter), according to the absorption and emission maximum of fluo-3 AM (506 and 526 nm, respectively). To assess intracellular calcium changes, the emission was monitored every 60 s for 15 min. Results are shown as the mean ± SEM of four independent experiments in six replicates and are expressed as percent of fluo-3 fluorescence compared with baseline of untreated cells. Calcium imaging experiments in TRPV-1 expressing CHO cells were performed at Eurofins S.A., using capsaicin (1 μM) as standard agonist.

Statistical Analyses. All values are expressed as mean ± SEM. Statistical analysis was performed by using GraphPad Prism 5 (GraphPad Software). Data were compared by independent Student's *t* test and analysis of variance (ANOVA). Multiple comparisons were conducted by one-way ANOVA followed by Tukey's test or two-way ANOVA followed by Bonferroni's test for multiple comparisons. $P < 0.05$ was considered significant.

1. Bíró T, Tóth BI, Haskó G, Paus R, Pacher P (2009) The endocannabinoid system of the skin in health and disease: Novel perspectives and therapeutic opportunities. *Trends Pharmacol Sci* 30(8):411–420.
2. Kendall AC, Nicolaou A (2013) Bioactive lipid mediators in skin inflammation and immunity. *Prog Lipid Res* 52(1):141–164.
3. Blankman JL, Cravatt BF (2013) Chemical probes of endocannabinoid metabolism. *Pharmacol Rev* 65(2):849–871.
4. Devane WA, et al. (1992) Isolation and structure of a brain constituent that binds to the cannabinoid receptor. *Science* 258(5090):1946–1949.
5. Piomelli D, Sasso O (2014) Peripheral gating of pain signals by endogenous lipid mediators. *Nat Neurosci* 17(2):164–174.
6. Karsak M, et al. (2007) Attenuation of allergic contact dermatitis through the endocannabinoid system. *Science* 316(5830):1494–1497.
7. Petrosino S, et al. (2010) Protective role of palmitoylethanolamide in contact allergic dermatitis. *Allergy* 65(6):698–711.
8. Pontis S, Ribeiro A, Sasso O, Piomelli D (2016) Macrophage-derived lipid agonists of PPAR-α as intrinsic controllers of inflammation. *Crit Rev Biochem Mol Biol* 51(1):7–14.
9. Saghatelian A, et al. (2004) Assignment of endogenous substrates to enzymes by global metabolite profiling. *Biochemistry* 43(45):14332–14339.
10. Saghatelian A, McKinney MK, Bandell M, Patapoutian A, Cravatt BF (2006) A FAAH-regulated class of N-acyl taurines that activates TRP ion channels. *Biochemistry* 45(30):9007–9015.
11. Reilly SJ, et al. (2007) A peroxisomal acyltransferase in mouse identifies a novel pathway for taurine conjugation of fatty acids. *FASEB J* 21(1):99–107.
12. Hunt MC, Siponen MI, Alexson SE (2012) The emerging role of acyl-CoA thioesterases and acyltransferases in regulating peroxisomal lipid metabolism. *Biochim Biophys Acta* 1822(9):1397–1410.
13. Chatzakos V, Slätis K, Djureinovic T, Helleday T, Hunt MC (2012) N-acyl taurines are anti-proliferative in prostate cancer cells. *Lipids* 47(4):355–361.
14. Waluk DP, Vielfort K, Derakhshan S, Aro H, Hunt MC (2013) N-acyl taurines trigger insulin secretion by increasing calcium flux in pancreatic β-cells. *Biochem Biophys Res Commun* 430(1):54–59.
15. Maccarrone M, et al. (2015) Endocannabinoid signaling at the periphery: 50 years after THC. *Trends Pharmacol Sci* 36(5):277–296.
16. Kathuria S, et al. (2003) Modulation of anxiety through blockade of anandamide hydrolysis. *Nat Med* 9(1):76–81.
17. Liang DY, et al. (2012) The complement component C5a receptor mediates pain and inflammation in a postsurgical pain model. *Pain* 153(2):366–372.
18. Sasso O, et al. (2012) Peripheral FAAH inhibition causes profound antinociception and protects against indomethacin-induced gastric lesions. *Pharmacol Res* 65(5):553–563.
19. Feingold K, Elias P (2014) The important role of lipids in the epidermis and their role in the formation and maintenance of the cutaneous barrier. *Biochim Biophys Acta* 1841(3):280–294.
20. Boccard J, Rutledge DN (2013) A consensus orthogonal partial least squares discriminant analysis (OPLS-DA) strategy for multiblock Omics data fusion. *Anal Chim Acta* 769:30–39.
21. Blasco H, et al. (2013) Metabolomics in cerebrospinal fluid of patients with amyotrophic lateral sclerosis: An untargeted approach via high-resolution mass spectrometry. *J Proteome Res* 12(8):3746–3754.
22. Saghatelian A, Cravatt BF (2005) Discovery metabolite profiling—Forging functional connections between the proteome and metabolome. *Life Sci* 77(14):1759–1766.
23. Martin P (1997) Wound healing—Aiming for perfect skin regeneration. *Science* 276(5309):75–81.
24. Michalik L, et al. (2001) Impaired skin wound healing in peroxisome proliferator-activated receptor (PPAR)alpha and PPARbeta mutant mice. *J Cell Biol* 154(4):799–814.
25. Wong VW, Sorkin M, Glotzbach JP, Longaker MT, Gurtner GC (2011) Surgical approaches to create murine models of human wound healing. *J Biomed Biotechnol* 2011:969618.
26. Liang CC, Park AY, Guan JL (2007) In vitro scratch assay: A convenient and inexpensive method for analysis of cell migration in vitro. *Nat Protoc* 2(2):329–333.
27. Singer AJ, Clark RA (1999) Cutaneous wound healing. *N Engl J Med* 341(10):738–746.
28. Hinz B (2007) Formation and function of the myofibroblast during tissue repair. *J Invest Dermatol* 127(3):526–537.
29. Morris VL, Chan BM (2007) Interaction of epidermal growth factor, Ca2+, and matrix metalloproteinase-9 in primary keratinocyte migration. *Wound Repair Regen* 15(6):907–915.
30. Elsholz F, Harteneck C, Muller W, Friedland K (2014) Calcium—A central regulator of keratinocyte differentiation in health and disease. *Eur J Dermatol* 24(6):650–661.
31. Downward J, Parker P, Waterfield MD (1984) Autophosphorylation sites on the epidermal growth factor receptor. *Nature* 311(5985):483–485.
32. Eming SA, Martin P, Tomic-Canic M (2014) Wound repair and regeneration: Mechanisms, signaling, and translation. *Sci Transl Med* 6(265):265sr6.
33. Raja, Sivamani K, Garcia MS, Isseroff RR (2007) Wound re-epithelialization: modulating keratinocyte migration in wound healing. *Front Biosci* 12:2849–2868.
34. Hinz B, et al. (2007) The myofibroblast: One function, multiple origins. *Am J Pathol* 170(6):1807–1816.
35. Bodnar RJ (2013) Epidermal growth factor and epidermal growth factor receptor: The yin and yang in the treatment of cutaneous wounds and cancer. *Adv Wound Care (New Rochelle)* 2(1):24–29.
36. Miyazaki A, Ohkubo T, Hatta M, Ishikawa H, Yamazaki J (2015) Integrin α6β4 and TRPV1 channel coordinately regulate directional keratinocyte migration. *Biochem Biophys Res Commun* 458(1):161–167.
37. Lo Verme J, et al. (2005) The nuclear receptor peroxisome proliferator-activated receptor-alpha mediates the anti-inflammatory actions of palmitoylethanolamide. *Mol Pharmacol* 67(1):15–19.
38. Solorzano C, et al. (2009) Selective N-acylethanolamine-hydrolyzing acid amidase inhibition reveals a key role for endogenous palmitoylethanolamide in inflammation. *Proc Natl Acad Sci USA* 106(49):20966–20971.
39. Zhu C, et al. (2011) Proinflammatory stimuli control N-acylphosphatidylethanolamine-specific phospholipase D expression in macrophages. *Mol Pharmacol* 79(4):786–792.
40. Sasso O, et al. (2013) Antinociceptive effects of the N-acylethanolamine acid amidase inhibitor ARN077 in rodent pain models. *Pain* 154(3):350–360.
41. Mor M, et al. (2004) Cyclohexylcarbamic acid 3′- or 4′-substituted biphenyl-3-yl esters as fatty acid amide hydrolase inhibitors: Synthesis, quantitative structure-activity relationships, and molecular modeling studies. *J Med Chem* 47(21):4998–5008.
42. Kovacs D, et al. (2012) The eumelanin intermediate 5,6-dihydroxyindole-2-carboxylic acid is a messenger in the cross-talk among epidermal cells. *J Invest Dermatol* 132(4):1196–1205.
43. Asada H, Linton J, Katz SI (1997) Cytokine gene expression during the elicitation phase of contact sensitivity: Regulation by endogenous IL-4. *J Invest Dermatol* 108(4):406–411.
44. Galiano RD, Michaels J, 5th, Dobryansky M, Levine JP, Gurtner GC (2004) Quantitative and reproducible murine model of excisional wound healing. *Wound Repair Regen* 12(4):485–492.
45. Gerharz M, et al. (2007) Morphometric analysis of murine skin wound healing: Standardization of experimental procedures and impact of an advanced multitissue array technique. *Wound Repair Regen* 15(1):105–112.
46. Brennan TJ, Vandermeulen EP, Gebhart GF (1996) Characterization of a rat model of incisional pain. *Pain* 64(3):493–501.
47. Bligh EG, Dyer WJ (1959) A rapid method of total lipid extraction and purification. *Can J Biochem Physiol* 37(8):911–917.
48. Wickramasekara SI, et al. (2013) Electrospray quadrupole travelling wave ion mobility time-of-flight mass spectrometry for the detection of plasma metabolome changes caused by xanthohumol in obese Zucker (fa/fa) rats. *Metabolites* 3(3):701–717.
49. González-Domínguez R, García-Barrera T, Vitorica J, Gómez-Ariza JL (2015) Deciphering metabolic abnormalities associated with Alzheimer's disease in the APP/PS1 mouse model using integrated metabolomic approaches. *Biochimie* 110:119–128.
50. Smith CA, et al. (2005) METLIN: A metabolite mass spectral database. *Ther Drug Monit* 27(6):747–751.
51. Tautenhahn R, et al. (2012) An accelerated workflow for untargeted metabolomics using the METLIN database. *Nat Biotechnol* 30(9):826–828.

52. Cajka T, Fiehn O (2014) Comprehensive analysis of lipids in biological systems by liquid chromatography-mass spectrometry. *Trends Analyt Chem* 61:192–206.

53. Vernez L, Hopfgartner G, Wenk M, Krähenbühl S (2003) Determination of carnitine and acylcarnitines in urine by high-performance liquid chromatography-electrospray ionization ion trap tandem mass spectrometry. *J Chromatogr A* 984(2):203–213.

54. Nichols KK, Ham BM, Nichols JJ, Ziegler C, Green-Church KB (2007) Identification of fatty acids and fatty acid amides in human meibomian gland secretions. *Invest Ophthalmol Vis Sci* 48(1):34–39.

55. Murphy RC, et al. (2005) Electrospray ionization and tandem mass spectrometry of eicosanoids. *Anal Biochem* 346(1):1–42.

56. Li NJ, et al. (2010) Plasma metabolic profiling of Alzheimer's disease by liquid chromatography/mass spectrometry. *Clin Biochem* 43(12):992–997.

57. Clapper JR, et al. (2010) Anandamide suppresses pain initiation through a peripheral endocannabinoid mechanism. *Nat Neurosci* 13(10):1265–1270.

58. Kovacs D, Cardinali G, Aspite N, Picardo M (2009) Bovine colostrum promotes growth and migration of the human keratinocyte HaCaT cell line. *Growth Factors* 27(6):448–455.